Contrib Mineral Petrol (2003) 146: 192–204
DOI 10.1007/s00410-003-0493-7

ORIGINAL PAPER

Dirk Frei · Axel Liebscher · Antje Wittenberg
Cliff S. J. Shaw

Crystal chemical controls on rare earth element partitioning between epidote-group minerals and melts: an experimental and theoretical study

Received: 29 November 2002 / Accepted: 5 June 2003 / Published online: 8 August 2003

Abstract We have experimentally determined the partitioning of REE (rare earth elements) between zoisite and hydrous silicate melt at 1,100 °C and 3 GPa. All REE behave moderately compatible in zoisite with respect to the melt and all $D_{REE}^{zo/melt}$ show a smooth parabolic dependence on ionic radius. The partitioning parabola peaks at Nd $\left(D_{Nd}^{zo/melt} = 4.9\right)$, and the compatibility slightly decreases towards La $\left(D_{La}^{zo/melt} = 3.9\right)$ and decreases by half an order of magnitude towards Yb $\left(D_{Yb}^{zo/melt} = 1.1\right)$. Application of the elastic strain model of Blundy and Wood (1994) to the available zoisite and allanite REE mineral/melt partitioning data and comparison with partitioning pattern calculated from a combination of structural and physical data (taken from the literature) with the elastic strain model suggest that in zoisite REE prefer the A1-site and that only La and Ce are incorporated into the A2-site in significant amounts. In contrast, in allanite, all REE are preferentially incorporated into the large and highly co-ordinated A2 site. As a result, zoisite fractionates the MREE effectively from the HREE and moderately from the LREE, while allanite fractionates the LREE very effectively from the MREE and HREE. Consequently, the presence of either zoisite or allanite during slab melting will lead to quite different REE pattern in the produced melt.

Editorial responsibility: J. Hoefs

D. Frei (✉)
Technische Universität Berlin, Fachgebiet Petrologie, Sekretariat BH1, Ernst-Reuter-Platz 1, 10587 Berlin, Germany
E-mail: df@geus.dk
Tel.: +45-3814-2263
Fax: +45-3814-2050

Present address: D. Frei
Geological Survey of Denmark and Greenland, Øster Voldgade 10, 1350 København K, Denmark

A. Liebscher
GeoForschungsZentrum Potsdam, Sektion 4.1, Experimentelle Geochemie und Mineralphysik, Telegrafenberg, 14473 Potsdam, Germany

A. Wittenberg
Institut für Mineralogie, Universität Hannover, Callinstr. 3, 30167 Hannover, Germany

C. S. J. Shaw
Bayerisches Geoinstitut, Universität Bayreuth, 95440 Bayreuth, Germany

Present address: C. S. J. Shaw
University of New Brunswick, Department of Geology, Fredericton, New Brunswick, E3B 5A3, Canada

Introduction

Epidote-group minerals are important rock forming minerals that exhibit diverse chemistry and occur in a wide variety of parageneses and geological settings. They are widespread in regional metamorphic rocks (from prehnite-pumpellyite to eclogite facies P–T conditions, Spear 1993; Poli and Schmidt 1998; Enami and Banno 1999), in metasomatic, hydrothermal and contact metamorphic rocks (Exley 1980; Peacor and Dunn 1988; Grew et al. 1991), and are common in veins, fissures, joint fillings, amygdales, and segregations (e.g., Pan and Fleet 1996; Brunsmann et al. 2000). Moreover, epidote-group minerals occur as magmatic phases in felsic igneous rocks (Zen and Hammarstrom 1984; Zen 1985; Evans and Vance 1987; Keane and Morisson 1997) and in pegmatites (Franz and Smelik 1995). Although the exact timing of magmatic epidote crystallization is debated (Zen 1985; Moench 1986; Tulloch 1986; Zen and Hammarstrom 1986; Franz and Smelik 1995; Keane and Morisson 1997), the available data favour a near solidus crystallization.

The wide range of occurrence of epidote-group minerals and their capacity to incorporate significant amounts of geochemically important trace elements such as Pb, Sr, U, Th, Y and the rare earth elements (REE) (e.g., Sakai et al. 1984; Grauch 1989; Sorensen 1991; Sorensen and Grossman 1993; Pan and Fleet 1996; Tribuzio et al. 1996; Carcangiu et al. 1997; Nagasaki and

Enami 1998; Brunsmann et al. 2000) underscores their importance for the chemical evolution of both mantle- and crustal-derived rocks. Recent studies on the trace element systematics of deeply subducted hydrous eclogites (Hermann 2002b; Zack et al. 2002) revealed that 80–90% of the bulk rock light rare earth elements (LREE = La to Nd) and 75% of the bulk rock U and Th are incorporated in zoisite and allanite. Both zoisite and allanite might be residual phases during low-degree partial melting of metabasalts and metasediments at temperatures critical for subduction zone melt extraction (Hermann and Green 2001; Hermann 2002a, 2002b; Skjerlie and Patino Douce 2002) and are thus capable of controlling the LREE and U and Th contents of melts generated in subduction zones.

Crucial for any quantitative description of the role of epidote-group minerals in REE fractionation processes, however, is a thorough understanding of their mineral/melt partitioning behaviour. Unfortunately, the available REE mineral/melt partitioning data for epidote-group minerals are limited to allanite either derived experimentally (Hermann 2002b) or from analyses of coexisting phenocryst-matrix pairs in silica-rich igneous rocks (Brooks et al. 1981; Mahood and Hildreth 1983; Sawka 1988). No mineral/melt partitioning data exist for zoisite, clinozoisite and epidote.

However, the change in crystal structure as a function of major element chemistry within the epidote-group (e.g., Dollase 1968, 1969, 1971; Gabe et al. 1973; Smyth and Bish 1988; Bonazzi and Menchetti 1995; Liebscher et al. 2002) and the principal lattice sites into which substitution of the REE takes place (Cressey and Steel 1988; Fleet and Pan 1995; Pan and Fleet 1996) are reasonably well understood. Since the incorporation of REE into crystals is dominantly controlled by space fitting requirements, the change in crystal structure within the epidote-group minerals is expected to have significant bearing on REE partitioning.

In this study, we present the first experimental data for the partitioning of REE (including Y) between zoisite and hydrous silicate melt. We combine the literature data on structural and physical properties of epidote-group minerals with the elastic strain model for trace element partitioning of Blundy and Wood (1994) and qualitatively predict the effects of crystal structure on REE partitioning. Based on these predictions, the available zoisite/melt and allanite/melt partitioning data, and the results of structure refinements of zoisite (Liebscher et al. 2002), we will discuss the site preference of REE in epidote-group minerals. This knowledge is important for the development of predictive models for REE mineral/melt partitioning because models using simplistic assumptions about REE incorporation and site occupancies in crystals might be erroneous (Bottazzi et al. 1999).

Crystal-chemical framework for the interpretation of REE behaviour in epidote-group minerals

In this study we focus on the orthorhombic member zoisite (zo) [$Ca_2Al_3(Si_3O_{11})(O/OH)$] and the monoclinic members clinozoisite (czo) [$Ca_2(Al,Fe^{3+})Al_2(Si_3O_{11})(O/OH)$], epidote (ep) [$Ca_2(Al,Fe^{3+})Al_2(Si_3O_{11})(O/OH)$], and allanite (all) [$(Ca,REE)_2(Fe^{2+},Fe^{3+},Al)_3(Si_3O_{11})(O/OH)$]. The epidote structure is composed of endless chains of edge-sharing octahedra parallel b that are cross-linked by isolated SiO_4 tetrahedra and Si_2O_7 groups (Fig. 1). Orthorhombic zoisite has only one type of chain with two non-equivalent octahedra M1,2 and M3 (Fig. 1a), whereas the monoclinic forms have two types of octahedra chains with three non-equivalent

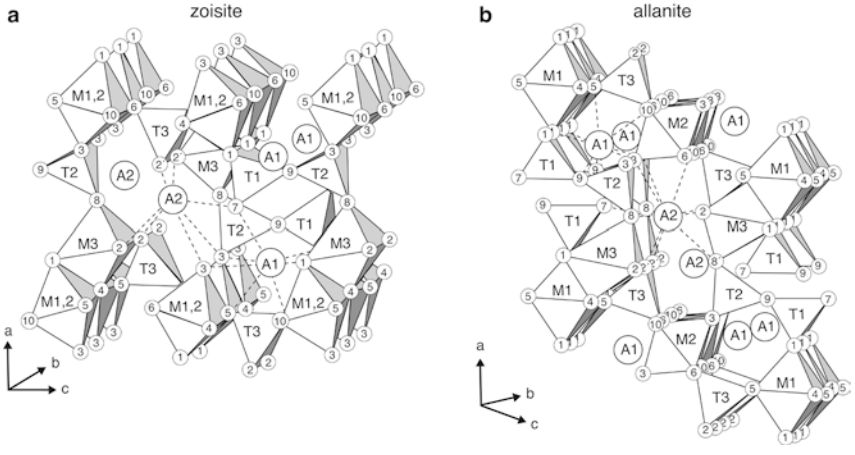

Fig. 1 Schematic sketches of **a** the orthorhombic zoisite and **b** monoclinic allanite structures. Both structures consist of endless octahedra chains parallel *b* that are cross-linked in *a* and *c* by isolated SiO_4 tetrahedral (*T3*) and Si_2O_7 groups (*T1*, *T2*). Zoisite has only one type of octahedra chain with two non-equivalent octahedra (*M1*, *M2* and *M3*), whereas allanite has two types of octahedra chains with three non-equivalent octahedra (*M1*, *M2*, *M3*). The large and irregular *A1* and *A2* sites, in which REE substitution takes place, are 7-fold co-ordinated in zoisite and 9-fold (*A1*) and 11-fold (*A2*) co-ordinated in allanite. In clinozoisite *A1* is 7-fold co-ordinated without the *A2*–O9 bonds of allanite, and *A2* is 8-fold coordinated without the *A2*–O8 and *A2*–O8́ bonds of allanite. In epidote *A1* is identical to A1 in allanite and A2 is 10-fold co-ordinated without the A2–O8́ bond of allanite (the hyphons at 08́ and O2́ refer to the bond lengths given in Table 4 and do not indicate non-equivalent O8 or O2 positions)

octahedra M1, M2 and M3 (Fig. 1b). The large irregular cavities between these cross-linked octahedra chains form the non-equivalent A1 and A2 polyhedra normally occupied by Ca. The smaller A1 site is seven-fold co-ordinated in zoisite and clinozoisite (Dollase 1968; Liebscher et al. 2002) and nine-fold co-ordinated in epidote and allanite (Dollase 1971). The larger A2 site is seven-fold co-ordinated in zoisite (Dollase 1968; Liebscher et al. 2002), eight-fold co-ordinated in clinozoisite (Dollase 1968), ten-fold co-ordinated in epidote (Dollase 1971), and 11-fold co-ordinated in allanite (Dollase 1971). The differences between the A-sites in zoisite and allanite are illustrated in Fig. 1.

Trivalent REE substitute for Ca on the A-sites (Dollase 1971; Bonazzi and Menchetti 1995; Pan and Fleet 1996) via coupled substitutions like

$$Ca^{2+}_{-1}Fe^{3+}_{-1}(REE)^{3+}_{+1}Fe^{2+}_{+1},$$

$$Ca^{2+}_{-1}+Al^{3+}_{-1}(REE)^{3+}_{+1}+Fe^{2+}_{+1}, \text{or}$$

$$Ca^{2+}_{-1}+Al^{3+}_{-1}(REE)^{3+}_{+1}+Mg^{2+}_{+1}.$$

Thus, the structural and physical properties of the A sites and their dependence upon major element chemistry will have a significant bearing on the REE fractionation by epidote-group minerals. Because the substitution of trace amounts of REE is unlikely to significantly change the geometry of the co-ordination polyhedra since the ionic radii of Ca and REE are very similar, the fractionation behaviour will be controlled by the overall structural differences between epidote-group minerals.

Crystal structure and prediction of REE partitioning pattern

To explore the effects of the changing structural environment of the A1 and A2 sites within the epidote-group on REE partitioning, we have applied the elastic strain model of Blundy and Wood (1994) to the structural and physical data reported in the literature for zoisite, clinozoisite, epidote, and allanite. For REE partitioning between epidote-group minerals and melts, Eq. (2) of Blundy and Wood (1994) can be rewritten into

$$D_{REE} = D_0^{3+}\left[\frac{-4\pi E^{3+}_{A1,A2}N_A}{RT}\left[\frac{r_0^{A1,A2}}{2}\left(r_{REE+Y}-r_0^{A1,A2}\right)^2 + \frac{1}{3}\left(r_{REE+Y}-r_0^{A1,A2}\right)^3\right]\right] \quad (1)$$

where D_0 is the strain free partition coefficient, N_A is Avogadrós Number, R is the gas constant, T is temperature in K, $r_0^{A1,A2}$ are the radii of the A1 and A2 site, r_{REE} are the ionic radii of REE, and $E^{3+}_{A1,A2}$ are the Youngs Moduli for the substitution of trivalent cations into the A1 or A2 site.

Using crystallographic data from the literature for zoisite (Liebscher et al. 2002), clinozoisite (Dollase 1968), epidote, and allanite (Dollase 1971) we have estimated values of $r_0^{A1,A2}$ $\left(r_0^{A1,A2} = d_{A1,A2} - r_{oxygen}\right)$ from the mean Ca-O distances assuming a radius for oxygen in 8-fold co-ordination of 1.42 Å (Shannon 1976). The ionic radii determined by Shannon (1976) have been used for r_{REE} in seven-, eight- and nine-fold co-ordination. Ionic radii for r_{REE} in 11-fold co-ordination have been graphically extrapolated from ionic radii for r_{REE} in 10- and 12-fold co-ordination (Shannon 1976). Values of $E^{3+}_{A1,A2}$ have been calculated as

$$E^{3+}_{A1,A2} = 1.5\left[750(\pm 20)\left(\frac{3}{d^3_{A1,A2}}\right)\right] \text{ GPa} \quad (2)$$

with d = mean Ca-O distance, according to the relationships between Young's modulus E, bulk modulus K, cation charge, and molecular volume established by Hazen and Finger (1979) and extended by Wood and Blundy (1997), assuming epidote-group minerals approximate Poisson solids with a Poisson ratio of 0.25.

In Eq. (1) all variables except the strain free partition coefficient for trivalent cations D_0^{3+} are intrinsic properties of the crystal and are not affected by the nature of the melt phase. Pressure and temperature control on REE partitioning appears in the P–T dependence of D_0^{3+} which varies according to the free energy of fusion of the host mineral end-member (Wood and Blundy 1997). Due to the absence of experimental partitioning data for epidote-group minerals it is impossible to constrain D_0^{3+} values independently and therefore only dimensionless REE partition coefficients can be obtained from Eq. (1).

Experimental and analytical techniques

Starting material

Zoisite can be regarded as the hydrated low-temperature, high-pressure equivalent of the anorthite component in metabasic rocks. To ensure anorthite saturation and promote growth of zoisite as a solidus phase, the starting material was prepared from a natural plagioclase cumulate of anorthositic composition (Se I, Table 1). The cumulate was ground and fused at 1,600 °C for ~1 h to obtain a homogeneous glass. This glass was ground under ethanol in an agate mortar to a fine-grained powder and subsequently doped with 500 ppm of La, Nd, Sm, Eu, Gd, Yb, and Y. All dopants were added as 99.9% pure oxides. The obtained powder was again fused at 1,600 °C for ~1 h, ground under ethanol in an agate mortar and dried. The resulting fine glass powder (Se I-d, Table 1) was used as starting material. The major and minor element composition, homogeneity, and absence of crystals of the starting material was checked by EMP. Trace element contents in the doped glass were controlled by inductively coupled plasma—mass spectrometry (ICP-MS).

Experimental procedure

Experiments were performed at 1,100 °C/3.0 GPa using a half-inch end-loaded piston cylinder apparatus at the Bayerisches Geoinstitut in Bayreuth with talc-pyrex assemblies with graphite furnaces and crushable alumina spacers. The starting material was contained in $Ag_{25}Pd_{75}$ capsules (4 mm outer diameter and length) placed along the vertical axis of the assembly. The temperature was

Table 1 Major, minor, and trace element composition of starting material

	Glass Se I (before doping)[a]	Glass Se I-d (after doping)[a]
Major and minor elements		
n[b]	18	10
wt%		
SiO_2	45.7 (2)	44.9 (3)
TiO_2	0.08 (3)	0.09 (2)
Al_2O_3	29.8 (3)	29.6 (1)
FeO	2.63 (15)	2.52 (4)
MnO	0.05 (3)	0.05 (1)
MgO	3.33 (9)	3.50 (7)
CaO	16.3 (2)	16.7 (1)
Na_2O	1.80 (11)	1.80 (7)
K_2O	0.13 (3)	0.12 (1)
Total	99.82	99.28
Trace elements		
n[b]	1	2
ppm		
La	1.15	451 (14)
Nd	1.5	445 (7)
Sm	0.31	450 (12)
Eu	0.21	438 (11)
Gd	0.35	432 (6)
Y	1.88	448 (3)
Yb	0.23	449 (3)

[a] 1σ standard deviation in parentheses refers to last digits
[b] n Number of analyses by EMP (major and minor elements) and ICP-MS (for trace elements)

controlled using a Pt-$Rh_{10}Pt_{90}$ thermocouple placed at the top of the capsule. No pressure correction was applied to thermocouple EMF. Based on calibrations against the albite-quartz-jadeite reaction and the kyanite-sillimanite transition, a 20% friction correction was applied for the talc-pyrex assemblies used in this study (for details see Shaw 1999). The oxidation fugacity for this assembly and the pressure and temperature applied in our experiments equals $\log f_{O2} = \mathrm{NNO}$. Run charges were brought to superliquidus conditions (1,400 °C) for 2 h and then cooled at a rate of 1 °C/min to the run temperature, at which they were kept for 184 h before quenching.

Analytical methods

The run products were analyzed by X-ray powder diffraction (STOE STADI P type) between 5 and 90° 2Θ with $CuK_{\alpha 1}$ radiation using a Ge(111) monochromator. The major and minor element composition of all phases (Table 2) were determined using a Cameca CAMEBAX EMP in wavelength dispersive mode. An accelerating voltage of 15 kV and a beam current of 18 nA were applied for major and minor element analyses. For mineral analysis, the beam diameter was 3 μm, while a slightly defocused beam of 5–10 μm was used for silicate glass analyses to minimise sodium migration during analysis. Because some of the zoisite crystals experimentally produced contained small inclusions of clinopyroxene and garnet up to 3 μm in size, the REE (and Y) concentrations in zoisite (Table 3) were also determined by EMP using the same equipment used for major- and minor-element analyses. REE analyses on zoisite were performed with 25 kV accelerating voltage and 100 nA beam current. A beam diameter of 3 μm was used to prevent concurrent analysis of mineral inclusions. Peak and background counting times were 20 and 10 s, respectively, for major and minor element analyses. For REE analyses, count rates were increased to 60 to 90 s and 30 to 45 s on the peak and background signal, respectively. Precision and accuracy of analysis are < 1% rel. for major elements, 5% rel. for minor elements and 20% rel. for REE.

Table 2 Major and minor element composition (wt%) of product phases as determined by EMP and calculated structural formulae of solid phases

	Grt[a]	Ky[a]	Cpx[a]	Zo[a]	Melt[a]
n[b]	24	5	14	23	6
SiO_2	40.2 (6)	36.8 (4)	49.0 (10)	39.2 (7)	53.9 (16)
TiO_2	0.12 (3)	0.03 (1)	0.10 (1)	0.06 (6)	0.16 (2)
Al_2O_3	24.1 (13)	62.8 (13)	18.9 (9)	32.7 (6)	18.8 (20)
FeO	7.4 (6)	0.36 (5)	1.95 (33)	–	1.05 (5)
Fe_2O_3	–	–	–	0.6 (2)	–
MnO	0.20 (5)	n.d.	0.05 (2)	0.02 (1)	0.05 (1)
MgO	7.7 (5)	0.08 (1)	7.9 (4)	0.30 (1)	1.8 (2)
CaO	19.9 (9)	0.14 (5)	18.3 (9)	24.7 (3)	11.5 (16)
Na_2O	0.06 (3)	0.01 (1)	3.1 (3)	0.05 (5)	2.4 (5)
K_2O	n.d.[c]	n.d.[c]	0.01 (1)	n.d.[c]	0.42 (7)
Total	99.59	100.11	99.38	97.56	90.03
Oxygens	12	5	6	12.5	
Si	2.97	1.02	1.75	2.99	
$Al^{[IV]}$	0.04	–	0.25	–	
$Al^{[VI]}$	2.06	1.95	0.55	2.94	
Ti	0.01	0.00	0.00	0.00	
Fe^{2+}	0.46	0.00	0.06	–	
Fe^{3+}	–	–	–	0.03	
Mn	0.01	0.00	0.00	0.00	
Mg	0.85	0.00	0.42	0.03	
Ca	1.57	0.01	0.70	2.02	
Na	0.01	0.00	0.21	0.01	
K	–	–	–	–	
Total	7.98	2.98	3.94	8.02	
vol%[d]	16	15	26	27	16

[a] 1σ standard deviation in parentheses refers to last digits
[b] n Number of analyses
[c] *n.d.* Not determined
[d] *vol%* Modal content calculated by least square regression of phase compositions and starting material

Table 3 Trace element composition (ppm) of zoisite and melt and calculated partition coefficients $D_{\mathrm{REE}}^{\mathrm{zo/melt}}$ and exchange coefficients $K_{\mathrm{D(REE1-REE2)}}^{\mathrm{zo/melt}}$

	Zoisite	Melt	$D_{\mathrm{REE}}^{\mathrm{zo/melt}}$[a]	$K_{\mathrm{D(REE1-REE2)}}^{\mathrm{zo/melt}}$[b]
n[c]	21	6		
La	1,030 (210)[d]	266 (12)	3.9 (8)	
Nd	1,080 (200)	220 (9)	4.9 (9)	
Sm	1,050 (230)	224 (15)	4.7 (11)	
Eu	990 (200)	241 (12)	4.1 (9)	
Gd	1,030 (210)	286 (15)	3.6 (8)	
Y	810 (360)	352 (17)	2.3 (10)	
Yb	590 (230)	560 (23)	1.1 (4)	
La–Yb				3.7 (16)
Sm–Yb				4.5 (20)
La–Sm				0.83 (26)

1σ standard deviation in parentheses refer to last digits
[a] $D_{\mathrm{REE}}^{\mathrm{zo/melt}} = \left(\frac{c_{\mathrm{REE}}^{\mathrm{zo}}}{c_{\mathrm{REE}}^{\mathrm{melt}}}\right)$
[b] $K_{\mathrm{D(REE1-REE2)}}^{\mathrm{zo/melt}} = \left(\frac{D_{\mathrm{REE1}}^{\mathrm{zo/melt}}}{D_{\mathrm{REE2}}^{\mathrm{zo/melt}}}\right)$
[c] n Number of analyses

Due to their concentrations close to or below the detection limit of the EMP, REE and Y contents in the melt (Table 3) were measured separately by laser ablation—inductively coupled plasma—mass spectrometry (LA-ICP-MS) at the University of Bristol. Analyses were carried out on the same polished, approximately 40-μm-thick section previously used for EMP analyses. LA-ICP-MS analyses were made using a frequency quadrupled New Wave

Research Nd-YAG laser emitting at 266 nm linked to a VG Elemental PlasmaQuad PQ3 S-Option ICP-MS instrument with a laser spot size of 10 μm. Typical 1σ precision is generally better than 5% relative and analyses of secondary standards (NIST SRM 612, BCR and BHVO) were consistently within 1σ of published working values.

Results

Description of run products

Two experimental runs with 0.2 and 2.0 wt% water added were performed. Because only one experiment (run 402 with 2 wt% H_2O added) yielded zoisite crystals suitable for REE determination (zoisite crystals in the other run were either too small or strongly poikilitic), we will only refer to this experiment in the following description: Run 402 consists of zoisite (zo), garnet (grt), kyanite (ky), clinopyroxene (cpx) and a hydrous silicate melt. Zoisite (orthorhombic symmetry confirmed by XRD) is 10 to 40 μm in size and usually inclusion free. Some crystals contain small inclusions of likely cpx or grt up to 3 μm in size (e.g., see large zoisite crystal at the bottom left corner in Fig. 2a) and these areas have been avoided for REE analysis by electron microprobe. Garnet is euhedral and strongly poikilitic and is up to ~30 μm in size (Fig. 2a). Kyanite and clinopyroxene form small (< 10 μm) anhedral crystals (Fig. 2a). The hydrous silicate melt is found as very thin seams around the solid phases and in a melt pool at the top of the capsule, a phenomenon often found in this kind of piston-cylinder experiments (Shaw 1999).

Phase compositions and volume proportions, calculated from least squares regression of phase compositions and starting materials, are listed in Table 2, REE contents in zoisite and melt in Table 3. Garnet (16 vol%) is grossular-rich (54 mol%) with 29 mol% pyrope and 16 mol% almandine component. Clinopyroxen (26 vol%) is iron-poor diopside with 23 mol% jadeite component. Zoisite (27 vol%) is nearly pure endmember with 0.59 wt% Fe_2O_3 (i.e., $X_{ps} = 0.03$) and 0.30 wt% MgO. REE contents range from 590 ppm Yb to 1,080 ppm Nd. The melt (16 vol%) has high Al_2O_3 (~19 wt%) and CaO (~11 wt%), intermediate SiO_2 (~54 wt%), and low FeO_{tot} (~1 wt%), MgO (~2 wt%), and total alkalis (~3 wt%) contents. Its REE contents range from 220 ppm Nd to 560 ppm Yb.

Although large and homogeneous zoisite crystals are notoriously difficult to grow due to sluggish reaction kinetics (cf. Brunsmann et al. 2002), the experimentally produced zoisite crystals are remarkably homogeneous. The observed chemical variations within individual crystals for major, minor, and rare earth elements are generally below the analytical precision. Furthermore, all of the partitioning data follow the parabolic dependence upon ionic radius predicted for equilibrium partitioning by Nagasawa (1966), Onuma et al. (1968), and Brice (1975) (Fig. 2b). We therefore conclude that our experiments offer a close approximation to equilibrium.

REE partitioning between zoisite and melt

REE concentrations of zoisite and melt and calculated partition coefficients (Table 3) show that all REE are moderately compatible. The compatibility increases by half an order of magnitude from Yb to Nd $\left(D_{Yb}^{zo/melt} = 1.1 \text{ to } D_{Nd}^{zo/melt} = 4.9\right)$ and slightly decreases towards La $\left(D_{La}^{zo/melt} = 3.9\right)$ (Fig. 2b). Despite their relatively large errors due to the precision of REE analyses in zoisite by EMP, all of the partitioning data display a smooth parabolic dependence of $D_{REE}^{zo/melt}$ upon ionic radius with the peak of the parabola at Nd (Fig. 2b). Fitting the data to the model of Blundy and Wood (1994) using a Levenberg-Marquardt-type,

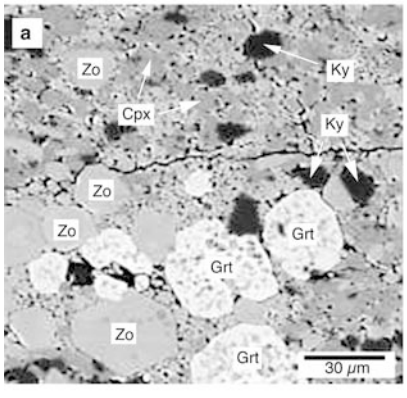

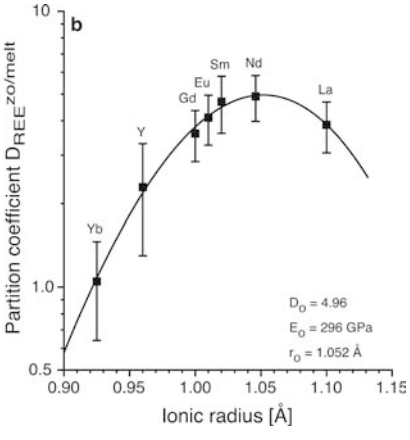

Fig. 2 **a** Secondary electron photomicrograph of run products in experimental run charge 402 (3 GPa/1,100 °C; 2 wt% H_2O added) showing euhedral zoisite (*zo*) and euhedral inclusion rich garnet (*grt*) in an interlocking matrix of subhedral clinopyroxene (*cpx*) and subhedral to euhedral kyanite (*ky*). Euhedral zoisite is up to 30 μm in size. Note that although some crystals contain small mineral inclusions, most zoisite crystals are inclusion free. **b** Onuma plot of the experimentally determined zoisite/melt REE partition coefficients (ionic radii are for seven-fold coordination; Shannon 1976). The *solid curve* represents the non-linear least square fit to Blundy and Wood's (1994) elastic strain model (fit parameters with errors are given in Table 5, *error bars* are 1 SD)

Table 4 Structural parameters of the A1 and A2 sites in zoisite, clinozoisite, epidote, and allanite (calculated and compiled after Dollase 1968, 1971; Liebscher et al. 2002) and calculated theoretical relative fractionation of the light, middle, and heavy REE between A1 and A2 sites, respectively, in zoisite, clinozoisite, epidote, and allanite and melt at 750 and 1,100 °C (see text)

Mineral	Zoisite (Liebscher et al. 2002)		Clinozoisite (Dollase 1968)		Epidote (Dollase 1971)		Allanite (Dollase 1971)	
Site	A1	A2	A1	A2	A1	A2	A1	A2
CN	VII	VII	VII	VIII	IX	X	IX	XI
Bond lengths (Å)								
A–O1 (2x)	2.457		2.490		2.465		2.373	
A–O2 (2x)		2.504		2.543		2.534		2.516
A–O2 (2x)		2.824		2.819		2.782		2.642
A–O3 (2x)	2.405	2.437	2.369	2.531	2.325	2.682	2.337	2.801
A–O5 (1x)	2.61		2.522		2.562		2.592	
A–O6 (1x)	2.57		2.745		2.885		2.911	
A–O7 (1x)	2.27	2.33	2.284	2.267	2.293	2.234	2.369	2.329
A–O8 (2x)						3.014		3.017
A–O8(1x)								3.127
A–O9 (2x)					3.007		3.112	
A–O10				2.575		2.529		2.611
Mean distance$d$ (Å)	2.453	2.551	2.467	2.579	2.593	2.679	2.613	2.729
r_0 (Å)[a]	1.033	1.131	1.047	1.159	1.173	1.259	1.193	1.309
Site volume V (Å^3)[b]	4.617	6.060	4.808	6.521	6.761	8.359	7.112	9.395
E (GPa)[c]	229 (6)	203 (5)	225 (6)	197 (5)	194 (5)	176 (5)	189 (5)	166 (4)
750 °C								
$K^{\mathrm{min/liq}}_{\mathrm{D(La-Yb)}}$ [d]	1.6	17	2.6	10	3.2	9.4	5.8	18
$K^{\mathrm{min/liq}}_{\mathrm{D(Sm-Yb)}}$ [d]	2.7	6.9	3.3	5.6	3.3	5.6	4.3	8.7
$K^{\mathrm{min/liq}}_{\mathrm{D(La-Sm)}}$ [d]	0.60	2.4	0.78	1.8	0.96	1.7	1.3	2.1
1,100 °C								
$K^{\mathrm{min/liq}}_{\mathrm{D(La-Yb)}}$ [d]	1.4	8.2	2.0	5.6	2.5	5.8	3.7	8.5
$K^{\mathrm{min/liq}}_{\mathrm{D(Sm-Yb)}}$ [d]	2.1	4.2	2.4	3.6	2.5	3.9	3.0	5.0
$K^{\mathrm{min/liq}}_{\mathrm{D(La-Sm)}}$ [d]	0.69	1.9	0.83	1.5	0.97	1.5	1.2	1.7

1σ standard deviation in parentheses refer to last digits

[a] $r_0 = d - 1.42$ (Å)

[b] $V = 4/3\pi {r_0}^3$

[c] $E = 3375(\pm 90)/d^3$ (GPa)

[d] $K^{\mathrm{min/liq}}_{\mathrm{D(REE1-REE2)}} = \exp\left[\frac{-4\pi E N_{\mathrm{A}}}{RT}\left[\frac{r_0}{2}\left(r^2_{\mathrm{REE2}} - r^2_{\mathrm{REE1}}\right) - \frac{1}{3}\left(r^3_{\mathrm{REE2}} - r^3_{\mathrm{REE1}}\right)\right]\right]$ with r_{REE} after Shannon (1976)

non-linear least squares fitting routine (Press et al. 1992) yields $D_0^{\mathrm{bulk}} = 4.96 \pm 0.54$, $E^{\mathrm{bulk}} = 296 \pm 83$ GPa, and $r_0^{\mathrm{bulk}} = 1.052 \pm 0.011$ Å (Fig. 2b).

To describe the relative fractionation of LREE, MREE (middle rare earth elements = Sm to Ho), and HREE (heavy rare earth elements = Er to Lu) between zoisite and melt we calculated the exchange coefficients $K^{\mathrm{zo/melt}}_{\mathrm{D(La-Yb)}}$, $K^{\mathrm{zo/melt}}_{\mathrm{D(Sm-Yb)}}$ and $K^{\mathrm{zo/melt}}_{\mathrm{D(La-Sm)}}$ $\left(K^{\mathrm{zo/melt}}_{\mathrm{D(i-j)}} = D^{\mathrm{zo/melt}}_{\mathrm{i}} / D^{\mathrm{zo/melt}}_{\mathrm{j}}\right)$; (Beattie et al. 1993). Zoisite effectively fractionates the LREE and MREE from HREE $\left(K^{\mathrm{zo/melt}}_{\mathrm{D(La-Yb)}} = 3.7 \pm 1.6 \text{ and } K^{\mathrm{zo/melt}}_{\mathrm{D(Sm-Yb)}} = 4.5 \pm 2.0\right)$ and slightly fractionates the MREE from LREE $\left(K^{\mathrm{zo/melt}}_{\mathrm{D(La-Sm)}} = 0.83 \pm 0.26\right)$ (Table 3).

Discussion

To interpret the experimental results in terms of REE site preference in zoisite and intracrystalline REE partitioning between zoisite A1 and A2 sites and to compare them with the partitioning behaviour of clinozoisite, epidote, and allanite, we calculated the theoretical dimensionless partition coefficients for REE incorporation into either the A1 or A2 sites of zoisite, clinozoisite, epidote, and allanite. These theoretical dimensionless partition coefficients allow the derivation of the principal differences in REE partitioning behaviour between the four modifications.

Theoretical prediction of dimensionless REE partition coefficients

The structural and physical parameters of the A1 and A2 sites in zoisite, clinozoisite, epidote, and allanite are given in Table 4 (compiled and calculated from Dollase 1968, 1971, Liebscher et al. 2002). In all four modifications the A2 site has a larger mean A–O distance d and a larger site volume V than the A1 site. The most interesting structural features with respect to REE incorporation are systematic changes in d and V between the four modifications. For both crystallographic sites these parameters continuously increase from zoisite to allanite by 0.16 Å for d^{A1}, 0.178 Å for d^{A2}, 2.495 Å^3 for V^{A1}, and 3.335 Å^3 for V^{A2}, respectively (Table 4). The increase in $d^{\mathrm{A1,A2}}$ from zoisite to allanite results in a concomitant increase in $r_0^{A1,A2}$ and decrease of $E^{\mathrm{A1,A2}}$ from zoisite to allanite (Table 4).

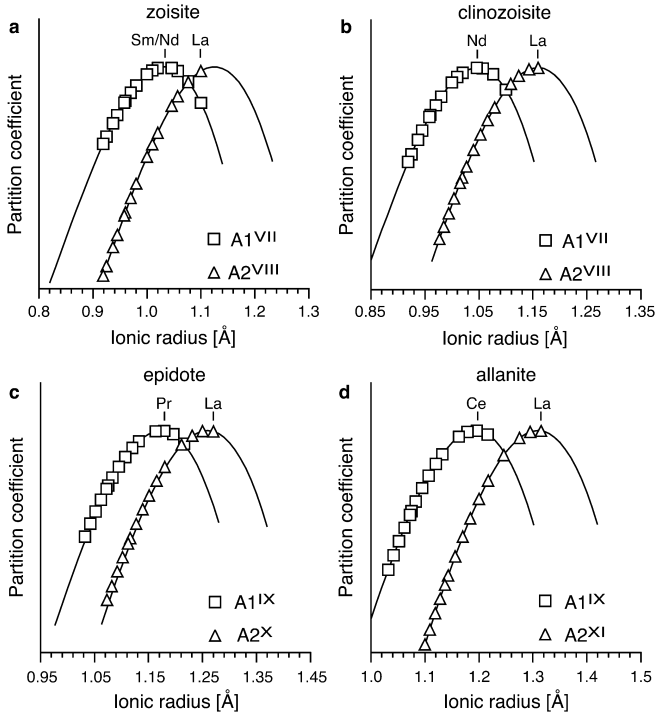

Fig. 3 Onuma plots of dimensionless REE partition coefficients, calculated from Eqs. (1) and (2) for substitution into the *A1* (*open symbols*) and *A2* (*filled symbols*) sites of **a** zoisite, **b** clinozoisite, **c** epidote, and **d** allanite. For partitioning into *A1* the peak position of the parabola shifts from *Sm/Nd* in zoisite to *Ce* in allanite. In contrast, for partitioning into *A2* the parabola consistently peaks at *La* for zoisite, clinozoisite, epidote, and allanite. Note the differences in coordination environment between *A1* and *A2* of zoisite, clinozoisite, epidote, and allanite. Ionic radii for REE in seven-, eight-, and nine-fold co-ordination are from Shannon (1976); ionic radii for REE in 11-fold co-ordination are extrapolated graphically from values for REE in 10- and 12-fold co-ordination (Shannon 1976)

The dimensionless REE partition coefficients for partitioning into A1 and A2 of zoisite, clinozoisite, epidote, and allanite, calculated with the data in Table 4, are plotted as a function of ionic radii in Fig. 3a–d. For partitioning into A1 the peak position of the parabola shows a systematic shift from Sm/Nd in zoisite to Nd in clinozoisite, Pr in epidote, and Ce in allanite corresponding to the systematic increase in r_0^{A1} from zoisite to allanite (Fig. 3). The increase in r_0^{A2} from zoisite to allanite is completely compensated by the change in the co-ordination environment (from 7-fold in zoisite to 8-fold in clinozoisite, 10-fold in epidote and 11-fold in allanite) and hence the partitioning parabola for incorporation into A2 generally peaks at La for all four modifications (Fig. 3).

Relative fractionation of LREE, MREE, and HREE

To evaluate the theoretical relative fractionation of LREE, MREE, and HREE for the partitioning into either A1 or A2 of zoisite, clinozoisite, epidote, and allanite and the influence of temperature, we have calculated the exchange coefficients $K_{D(La-Yb)}^{zo/melt}$, $K_{D(Sm-Yb)}^{zo/melt}$, and $K_{D(La-Sm)}^{zo/melt}$ by applying Eq. (1) for $T = 750$ and 1,100 °C (Table 4). The exchange coefficients are independent upon the strain free partition coefficient D_0, and hence independent upon the absolute concentrations of La, Sm, and Yb in coexisting mineral and melt.

The shift of the peak of the partitioning parabola for partitioning into A1 from Sm/Nd (zo) to Nd (czo), Pr (ep), and Ce (all) (Fig. 3) is mirrored by different relative fractionation behaviours of the four modifications. Zoisite will be enriched in the MREE compared to the heavy and light REE $\left(K_{D(Sm-Yb)}^{zo(A1)/melt} \sim 2to3,\ K_{D(La-Sm)}^{zo(A1)/melt} \sim 0.6to0.7\right)$ and will only show a modest enrichment of the LREE over the HREE $\left(K_{D(La-Yb)}^{zo(A1)/melt} \sim 1.5\right)$. Clinozoisite and epidote will show an overall enrichment of the light and middle REE over the heavy REE with La/Yb and Sm/Yb ratios about two to three times higher than in the coexisting melt. However, with La/Sm ratios of about 0.8 to 1.0 times that in the coexisting melt they will slightly fractionate the middle REE from the light REE. Allanite will fractionate the light and middle REE from the heavy REE with an about 4- to 6-times higher La/Yb ratio and three to four times higher Sm/Yb ratio than the coexisting melt. With a La/Sm ratio of about 1.2 to 1.3 times that of the coexisting melt it will also slightly fractionate the light from the middle REE.

In contrast, for partitioning into the A2 site, all four modifications will fractionate the light from the middle and heavy REE. This fractionation is the smallest in clinozoisite and epidote and both are comparable in their fractionation behaviour. They will have an about five to ten times higher La/Yb, an about three to six times higher Sm/Yb ratio, and an about 1.5 to 1.8 times higher La/Sm ratio than the coexisting melt. Surprisingly, zoisite and allanite show an almost identical fractionation behaviour for A2. They will have an about 8 to 20 times higher La/Yb, 4 to 9 times higher Sm/Yb ratio, and 1.7 to 2.5 times higher La/Sm ratio than the coexisting melt.

As one would expect, the principal partitioning behaviour of the A1 and A2 sites of the four modifications is independent upon temperature. Temperature only affects the degree of relative fractionation of LREE, MREE, and HREE, with relative fractionation most pronounced at low temperature and weakest at high temperature (Table 4).

REE site location in zoisite

A comparison of the partitioning parabola fitted to the experimental data (Fig. 2b; Table 5) with the theoretical partitioning parabola for the A1 and A2 sites in zoisite (Fig. 3a; Table 5) indicates that the experimentally

Table 5 Parameters r_o, E, D_o, and exchange coefficients $K^{zo/melt}_{D(REE1-REE2)}$ from theory, experiment, and calculation

	A1 (theory)	A2 (theory)	Zoisite bulk (experiment)	A1 (experiment)	A2 (experiment)
r_0 (Å)	1.033[a]	1.131[a]	1.052 (11)	1.033[a]	1.131[a]
E (GPa)	229 (6)[a]	203 (6)[a]	296 (83)	377 (2)	223 (2)
D_0	/	/	4.96 (54)	3.82 (1)	1.97 (1)
$K^{zo/melt}_{D(La-Yb)}$ [b]	1.4	8.2	3.7 (16)	2.2	21
$K^{zo/melt}_{D(Sm-Yb)}$ [b]	2.1	4.2	4.5 (20)	4.0	8.6
$K^{zo/melt}_{D(La-Sm)}$ [b]	0.69	1.9	0.83 (26)	0.56	2.4

1σ standard deviation in parentheses refer to last digits
[a]Taken from Table 4, not fitted
[b]$K^{zo/melt}_{D(REE1-REE2)} = \left(\frac{D^{zo/melt}_{REE1}}{D^{zo/melt}_{REE2}}\right)$
1σ standard deviation in parentheses refer to last digits

determined partitioning data can not be explained with exclusive ordering of REE into either A1 or A2. With $r_0 = 1.052$ Å the experimental parabola peaks between the theoretical values for A1 $\left(r_0^{A1} = 1.033\text{Å}\right)$ and A2 $\left(r_0^{A2} = 1.131\text{Å}\right)$. A combined contribution of A1 and A2 to the observed partitioning is also supported by the relative fractionation of La, Sm, and Yb. The experimentally determined $K^{zo/melt}_{D(La-Yb)} = 3.7$ and $K^{zo/melt}_{D(La-Sm)} = 0.83$ are between those expected for exclusive partitioning into either A1 $\left(K^{zo(A1)/melt}_{D(La-Yb)} = 1.4,\ K^{zo(A1)/melt}_{D(La-Sm)} = 0.69\right)$ or A2 $\left(K^{zo(A2)/melt}_{D(La-Yb)} = 8.2,\ K^{zo(A2)/melt}_{D(La-Sm)} = 1.9\right)$ (Table 5). To resolve the contributions of A1 and A2 to the observed bulk-partitioning pattern, and to determine the intracrystalline REE partitioning between A1 and A2, we have fitted our experimentally derived partition coefficients with two parabolas for A1 and A2, respectively. Because $D^{zo(bulk)/melt}_{REE} = D^{zo(A1)/melt}_{REE} + D^{zo(A2)/melt}_{REE}$ and taking $r_0^{A1,A2}$ from Table 4, the data can be fitted to

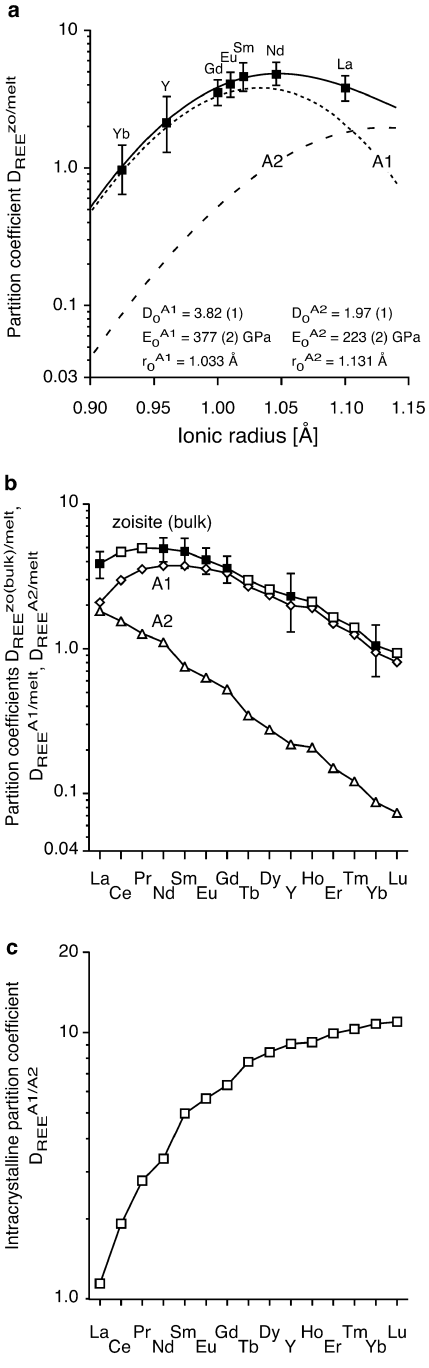

Fig. 4 **a** Onuma plot of the experimentally determined zoisite/melt REE partition coefficients. The *solid line* represents the weighted non-linear least square fit to Blundy and Wood's (1994) elastic strain model; the *dotted* and the *dashed line* represent the contributions of the *A1* and *A2* sites in zoisite, respectively, to the observed bulk partitioning behaviour (see text for details; fit parameters with errors are given in Table 5); **b** partition coefficients $D^{zo(bulk,A1,A2)/melt}_{REE}$ showing the REE patterns of zoisite (bulk) and of the *A1* and *A2* sites compared to the melt. Zoisite will be overall enriched in the light and middle REE compared to the melt with maximum enrichment for *Nd*. *A1* displays a MREE-enriched pattern, whereas *A2* has a straight, LREE-enriched one. Except *Yb* and *Lu* all REE are compatible with respect to *A1*, whereas only *La* to *Nd* are compatible with respect to *A2*. *Filled symbols* indicate experimentally determined values (presented in Table 3) whereas *empty symbols* indicate values calculated (using data from Tables 4, 5) and presented in Table 6; **c** intracrystalline partition coefficients $D^{A1/A2}_{REE}$ (Table 6) calculated according to the data in Tables 5, 6. All REE favour the *A1* site of zoisite. This preference for *A1* over *A2* increases by one order of magnitude with decreasing ionic radius (*error bars* denote 1σ standard deviation; ionic radii are from Shannon 1976 for seven-fold coordination; exchange coefficients $K^{zo(A1,A2)/melt}_{D(REE1-REE2)}$ describing the relative fractionation of the light, middle, and heavy REE for all Onuma plots are listed in Table 5)

$$D_{\mathrm{REE}}^{\mathrm{zo(bulk)/melt}} = D_0^{A1}\exp\left[\frac{-4\pi E^{A1}N}{RT}\left[\frac{1.033}{2}(r_{REE}-1.033)^2 + \frac{1}{3}(r_{REE}-1.033)^3\right]\right] + D_0^{A2}\exp\left[\frac{-4\pi E^{A2}N}{RT}\left[\frac{1.131}{2}(r_{REE}-1.131)^2 + \frac{1}{3}(r_{REE}-1.131)^3\right]\right]. \quad (3)$$

The resulting fit is displayed in Fig. 4a and the derived parameters for A1 and A2 are listed in Table 5. The strain-free partition coefficient D_0 for A1 $\left(D_0^{\mathrm{A1}} = 3.82\right)$ is about twice as much for A2 $\left(D_0^{\mathrm{A2}} = 1.97\right)$, indicating that the REE are preferentially incorporated into A1. Combining the strain free partition coefficients with the strain free radii $r_0^{\mathrm{A1,A2}}$ the data show the bulk partitioning behaviour of the middle and heavy REE is almost exclusively controlled by A1 and A2 significantly contributes only to the bulk partitioning of La, Ce, and Pr (Fig. 4). The derived $E^{\mathrm{A1}} = 377$ GPa and $E^{\mathrm{A2}} = 223$ GPa are larger than those theoretically predicted (Table 5). Varying $D_{\mathrm{REE}}^{\mathrm{zo(bulk)/melt}}$ within their errors (Table 3) and fitting to Eq. (1) shows that E is very sensitive to even smallest changes in $D_{\mathrm{REE}}^{\mathrm{zo(bulk)/melt}}$ and its error is probably in the range of ± 100 GPa. Bearing in mind that the calculation of E from the interatomic distances assumes a spherical coordination shell, what is surely not true for the A1 and A2 sites of zoisite, the theoretically predicted and the calculated E^{A1} and E^{A2} are at least of the same order of magnitude. Independent upon the absolute values for E^{A1} and E^{A2}, both methods agree in $E^{\mathrm{A1}} > E^{\mathrm{A2}}$ (Table 5).

Taking the fitted values for $D_0^{\mathrm{A1,A2}}$ and $E^{\mathrm{A1,A2}}$, and the values for $r_0^{\mathrm{A1,A2}}$ from the crystallographic data (Tables 4, 5), we have calculated the partition coefficients for the REE between the A1 and A2 sites in zoisite and siliceous melt as well as the intracrystalline partitioning of the REE between A1 and A2 (Table 6; Fig. 4b, c). A1 displays a MREE-enriched REE pattern compared to the melt whereas A2 displays a straight LREE-enriched pattern. In the case of A1, all REE except Yb and Lu are compatible with respect to the melt, whereas in the case of A2 only La to Nd are compatible (Table 6; Fig. 4b). The intracrystalline REE partitioning between A1 and A2 is in favour for A1 for all REE and increases continuously from $D_{\mathrm{La}}^{\mathrm{A1/A2}} = 1$ to $D_{\mathrm{Lu}}^{\mathrm{A1/A2}} = 11.0$ (Table 6; Fig. 4c). This is in marked contrast to monoclinic epidote and allanite in which the REE show a strong, almost exclusive preference for the A2 site (Dollase 1971; Cressey and Steel 1988; Bonazzi and Menchetti 1995; Bonazzi et al. 1996, this study, see below). The data of Cressey and Steel (1988) indicate that in REE-rich epidote (i.e., ΣREE A2 > 0.9 cations per formula unit), the light and middle REE are exclusively incorporated on A2, whereas only the HREE show a preference for A1 with Lu maybe entering even the M3 octahedron.

Table 6 $D_{\mathrm{REE+Y}}^{\mathrm{zo(bulk)/melt}}$, $D_{\mathrm{REE+Y}}^{\mathrm{zo(A1)/melt}}$, and $D_{\mathrm{REE+Y}}^{\mathrm{zo(A2)/melt}}$ partition coefficients, REE + Y concentrations (ppm) on A1 and A2, and intracrystalline partition coefficients $D_{\mathrm{REE+Y}}^{\mathrm{A1/A2}}$

	$D_{\mathrm{REE+Y}}^{\mathrm{zo(bulk)/melt}}$	$D_{\mathrm{REE+Y}}^{\mathrm{zo(A1)/melt}}$	$D_{\mathrm{REE+Y}}^{\mathrm{zo(A2)/melt}}$	$c_{\mathrm{REE+Y}}^{\mathrm{A1}}$ [a]	$c_{\mathrm{REE+Y}}^{\mathrm{A2}}$ [a]	$D_{\mathrm{REE+Y}}^{\mathrm{A1/A2}}$ [b]
La	3.87[c]	2.09	1.82	555	484	1.15
Ce	4.66	2.97	1.55			1.92
Pr	4.95	3.54	1.27			2.79
Nd	4.91[c]	3.74	1.11	822	244	3.37
Sm	4.7[c]	3.74	0.75	837	169	4.97
Eu	4.11[c]	3.57	0.63	861	152	5.65
Gd	3.60[c]	3.33	0.52	952	150	6.35
Tb	2.98	2.69	0.35			7.75
Dy	2.57	2.34	0.28			8.43
Y	2.3[c]	1.98	0.22	698	77	9.07
Ho	2.10	1.91	0.21			9.19
Er	1.65	1.49	0.15			9.92
Tm	1.40	1.25	0.12			10.3
Yb	1.05[c]	0.94	0.087	527	49	10.8
Lu	0.93	0.81	0.074			11.0

[a] $c_{\mathrm{REE+Y}}^{\mathrm{A1,A2}} = D^{\frac{\mathrm{zo(A1,A2)/melt}}{\mathrm{REE+Y}}} * c_{\mathrm{REE+Y}}^{\mathrm{melt}}$

[b] $D_{\mathrm{REE+Y}}^{\mathrm{A1/A2}} = \frac{D^{\frac{\mathrm{zo(A1)/melt}}{\mathrm{REE+Y}}}}{D^{\frac{\mathrm{zo(A2)/melt}}{\mathrm{REE+Y}}}}$

[c] Calculated from the experimental data, all other values are calculated based on the crystallographic values for $r_0^{\mathrm{A1/A2}}$ and the fitted values for $r_0^{\mathrm{zo(bulk)}}$, $E^{\mathrm{zo(bulk),A1,A2}}$, and $D_0^{\mathrm{zo(bulk),A1,A2}}$ (Table 5)

Comparison with natural REE bearing zoisites

The principal characteristics of the fractionation of the REE by zoisite with preferred incorporation of the middle and, to a lesser extent, light REE in zoisite compared to the heavy REE (Fig. 2b) agree well with REE patterns of natural zoisite. Sorensen and Grossman (1989) and Hickmott et al. (1992) published zoisite REE patterns from garnet amphibolites from Catalina Schist, southern California, that show MREE > LREE > HREE. Normalized to primitive mantle values, their data suggest relative fractionation between the LREE, MREE, and HREE by zoisite of ~14 for La/Yb, ~17 for Sm/Yb, and ~0.9 for La/Sm (Sorensen and Grossman 1989) and of ~6 for Ce/Yb, ~10 for Sm/Yb, and ~0.6 for Ce/Sm (Hickmott et al. 1992) in fairly good agreement with the exchange coefficients determined in this study (Table 5). Igneous zoisites from high-pressure pegmatites from the Münchberg Massif, Central Europe Variscan Belt, and the Saualpe, Austria, are characterized by an enrichment of the light and middle REE relative to HREE and almost identical concentrations of the light and middle REE (Franz, personal communication). Such a lack of relative fractionation between the light and middle REE is consistent with a combined contribution of A1 and A2 of zoisite to the REE fractionation behaviour as determined here.

Clinozoisite/melt and epidote/melt REE partitioning

Due to the lack of experimental or natural partitioning data for the REE between either clinozoisite or epidote and melt, we neither can test the theoretical partitioning patterns nor can we extract site occupancy data for the REE in clinozoisite and epidote. However, some general conclusions may be drawn from published REE patterns in natural clinozoisite and epidote from igneous and metamorphic rocks. The theoretical REE patterns for clinozoisite and epidote indicate that, for an exclusive crystal chemical control on the REE fractionation behaviour of clinozoisite and epidote, partitioning into A2 should result in straight, LREE-enriched patterns for both minerals compared to the coexisting phase, whereas partitioning into A1 should be mirrored by overall light and middle REE-enriched patterns but with a slight enrichment of the middle REE over the light REE (Fig. 2b, c). This slight enrichment of the middle over the light REE should be especially true for clinozoisite.

REE patterns of clinozoisite are only rarely reported and yield ambiguous results. Sorensen and Grossman (1989) published a clinozoisite REE pattern that is LREE-enriched and has a La/Sm ratio >1, whereas Pan and Fleet (1996) published a clinozoisite pattern that is straight HREE enriched with La/Yb = 0.09. Some hints to the REE fractionation behaviour of clinozoisite come from clinozoisite from high-pressure segregations that formed by the breakdown of zoisite (Liebscher, unpublished data) and from coexisting clinozoisite and zoisite from high-pressure pegmatites (Franz, personal communication). In these samples, the clinozoisite REE patterns are comparable to those of zoisite, suggesting that no significant fractionation of the REE occurs between clinozoisite and zoisite and that clinozoisite also favour an incorporation of the middle REE. Such a preferred incorporation of the middle REE in clinozoisite requires a significant contribution of A1 to the REE incorporation (Fig. 2b).

With only a few exceptions, published REE patterns of epidote generally show straight, LREE-enriched patterns (Nystrom 1984; Carcangiu et al. 1997; Sorensen and Grossman 1993; Exley 1980; Bonazzi and Menchetti 1995) with positive La/Sm ratios, thus pointing to incorporation of the REE in A2, which would be consistent with the REE site occupancy in REE-rich epidote as determined by Bonazzi and Menchetti (1995).

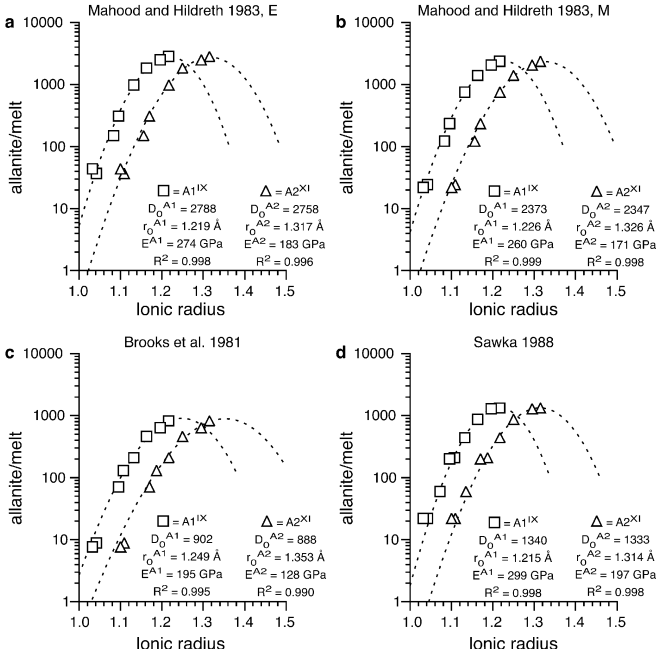

Fig. 5 Onuma plots of allanite/melt REE partition coefficients from Mahood and Hildreth (1983) (**a, b**), Brooks et al. (1981) (**c**), and Sawka (1988) (**d**) (ionic radii are for 9-fold co-ordination (*A1*) and 11-fold coordination (*A2*), respectively; Shannon 1976). *Solid curves* are non-linear least square fits to Blundy and Wood's (1994) elastic strain model (fit parameters with errors are given in Table 7); *E* and *M* correspond to samples E and M, respectively, of Mahood and Hildreth 1983)

Allanite/melt REE partitioning

To compare the theoretical dimensionless REE partitioning patterns for allanite A1 and A2 sites (Fig. 3d)

Table 7 Fitted values for the strain free partition coefficient $D_0^{A1,A2}$, strain-free radius $r_0^{A1,A2}$, and the Youngs Modulus $E^{A1,A2}$ and relative fractionation of the light, middle, and heavy REE between allanite and melt for published allanite/melt partition coefficients

Source	Mahood and Hildreth 1983, E		Mahood and Hildreth 1983, M		Brooks et al. 1981		Sawka 1988		Mean	
Site	A1	A2	A1	A2	A1	A2	A1	A2	A1	A2
CN	IX	XI	IX	XI	IX	XI	IX	XI	IX	XI
$D_0^{A1,A2}$	2788 (67)[a]	2758 (85)	2373 (48)	2347 (75)	902 (124)	888 (170)	1340 (24)	1333 (29)		
$r_0^{A1,A2}$	1.219 (5)	1.317 (8)	1.226 (4)	1.326 (8)	1.249 (21)	1.353 (35)	1.215 (4)	1.314 (5)	1.227 (15)	1.328 (18)
$E^{A1,A2}$	274 (31)	183 (30)	260 (20)	171 (22)	195 (54)	128 (50)	299 (25)	197 (23)	257 (44)	170 (30)
$K_{D(La-Yb)}^{all/melt}$	76 (3)		96 (24)		92 (21)		60 (9)		81 (16)	
$K_{D(La-Sm)}^{all/melt}$	2.9 (1)		3.1 (1)		3.9 (3)		3.0 (3)		3.2 (5)	
$K_{D(Sm-Yb)}^{all/melt}$	26 (1)		31 (8)		24 (5)		20 (3)		25 (5)	

1σ standard deviation in parentheses refer to last digits

with natural mineral/melt partitioning data (Brooks et al. 1981; Mahood and Hildreth 1983; Sawka 1988), we have plotted the published partition coefficients versus ionic radii, assuming exclusive substitution into either the A1 or A2 site, and fitted them to Eq. (2) of Blundy and Wood (1994) to derive best fit values for $D_0^{A1,A2}$, $r_0^{A1,A2}$, and $E^{A1,A2}$ using a Levenberg-Marquardt-type, non-linear least squares fitting routine (Press et al. 1992, Fig. 5, Table 7). Despite minor differences, all four data sets agree in their principal characteristics. For partitioning into A1 the data suggest a relatively high Youngs modulus E^{A1} of 257 ± 44 GPa and a strain-free radius r_0^{A1} of 1.227 ± 0.015 Å (Fig. 5; Table 7). For partitioning into A2 they suggest a smaller Young's modulus E^{A2} of only 170 ± 30 GPa and a larger strain-free radius r_0^{A2} of 1.328 ± 0.018 Å (Fig. 5; Table 7). The differences in $D_0^{A1,A2}$ between the four data sets (Table 7) most probably reflect differences in melt composition and P–T conditions of crystallization. The overall relative fractionation of the light, middle, and heavy REE between allanite and melt is also comparable in the four data sets, suggesting that all represent an identical substitution mechanism of the REE in allanite. With $K_{D(La-Yb)}^{all/melt} = 81 \pm 16$ and $K_{D(La-Sm)}^{all/melt} = 3.2 \pm 0.5$, the LREE are strongly fractionated by allanite from the middle and heavy REE (Table 7).

The results obtained from natural mineral/melt partitioning data show a good agreement with those predicted theoretically for partitioning into A2. Like the theoretical partition parabola for A2 (Fig. 3d) all parabola to the natural allanite/melt partitioning data peak at La and give no hints to a preferred incorporation of Ce (Fig. 5) as would be expected for partitioning into A1 (Fig. 3d). Additionally, the fitted values for E^{A2} of 170 ± 30 GPa and r_0^{A2} of 1.328 ± 0.018 Å (Table 7) are within error comparable to those predicted from crystallographic data ($E^{A2} = 166$ GPa, $r_0^{A2} = 1.309$ Å; Table 4). In contrast, the fitted values for E^{A1} ($= 257 \pm 44$ GPa; Table 7) and r_0^{A1} ($= 1.227 \pm 0.015$ Å); Table 7) significantly deviate from those theoretically predicted ($E^{A1} = 189$ GPa, $r_0^{A1} = 1.193$ Å; Table 4). The data therefore strongly suggest an incorporation of the REE into the A2 site in allanite. One difference between the theoretically predicted and measured partitioning patterns is the slightly different relative fractionation of the light, middle, and heavy REE. $K_{D(La-Yb)}^{all/melt}$, $K_{D(La-Sm)}^{all/melt}$ and $K_{D(Sm-Yb)}^{all/melt}$ determined from the published partitioning data are about 1.5 to 4.5 times higher than those theoretically predicted (Tables 4, 7). The reason for this is the sensitivity of Eq. (1) to even smallest changes of E and r_0. Varying E and r_0 within only ± 20 GPa and ± 0.02 Å results in a range of theoretical fractionation behaviours that covers those determined from the literature data.

Incorporation of the REE into the A2 site of allanite, as suggested by the above discussion, is in good agreement with published REE pattern of allanite and studies on the site location of the REE in allanite. All published REE patterns of allanite show strong LREE enrichment compared to MREE and HREE (e.g., Henderson 1982; Sorensen and Grossman 1989; Hermann 2002b). Structure refinements of allanite suggest that the REE order at the larger A2 site (Dollase 1971; Bonazzi and Menchetti 1995). Results from EXAFS spectroscopic studies on dissakisite, the Mg end member of allanite, demonstrate that REE are exclusively incorporated into the A2 site (Cressey and Steel 1988). Smyth and Bish (1988) found that A2 in allanite has a much deeper electrostatic energy potential than A1 and concluded that this accounts for the preference of REE for the A2 over the A1 site in allanite and may explain the large observed allanite/melt partition coefficients.

In a recent contribution, Hermann (2002b) reported the first experimentally determined data for REE partitioning between allanite and a hydrous granitic melt at 900 °C and 2 GPa. Compared to the natural allanite/melt partitioning data and the predicted partitioning pattern, the data reported by Hermann (2002b) display some striking differences. The absolute values of $D_{LREE}^{all/melt}$ are one order of magnitude lower while the absolute values of $D_{HREE}^{all/melt}$ are one order of magnitude higher than the reported natural allanite/melt partitioning data. This results, within error, in an overall flat partitioning pattern with no fractionation of LREE from MREE $\left(D_{La}^{all/melt} \text{ to } D_{Dy}^{all/melt} \approx 210 \pm 20; K_{D(La-Sm)}^{all/melt} = 1.1\right)$ and only weak fractionation of LREE and MREE from HREE $\left(K_{D(La-Yb)}^{all/melt} = 2.1 \text{and} K_{D(Sm-Yb)}^{all/melt} = 1.9\right)$. In an Onuma plot, the partitioning data do not show a smooth parabolic dependence on ionic radius. A fit of the partitioning data to Blundy and Woods (1994) elastic strain model, assuming exclusive substitution into either the A1 or A2 site yields best-fit values of r_0^{A1} $\left(= 1.161 \pm 0.008 \text{ Å}\right)$, $r_0^{A2}\left(= 1.251 \pm 0.008 \text{Å}\right)$,, E^{A1} ($= 1.400 \pm 220$ GPa), and E^{A2} ($= 760 \pm 120$ GPa) that are crystallographically and physically unrealistic (Grevel et al. 2000 and references therein). To resolve the observed discrepancy between the experimentally produced partitioning data and the natural partitioning data more experimental work is necessary which is beyond the scope of this contribution.

Conclusions

This study reports experimentally derived data for the partitioning of REE between zoisite and hydrous silicate melt at pressure and temperature conditions relevant to slab melting. The combination of this experimentally derived data and natural allanite/melt partitioning data with theoretical models for trace element partitioning and structural considerations based on precise crystal-structural data allows to unravel the complex REE incorporation mechanisms in zoisite and allanite. In zoisite, the quantitative and qualitative most important substitution of REE takes place into the A1 site and not

into the A2 site. This is in marked contrast to allanite, where REE are exclusively incorporated into the A2 site. As a consequence, zoisite effectively fractionates the MREE from the HREE and moderately from the LREE (comparable to apatite and sphene; Sorensen and Grossman 1989; Hickmott et al. 1992), while allanite fractionates the LREE very effectively from the MREE and HREE. For subduction zone processes, this means that slab melting will result in melts that are depleted in MREE if zoisite is a liquidus phase and will be MREE enriched if zoisite is consumed during dehydration melting. The replacement of zoisite as a major rock-forming mineral in subducted crust by allanite as an accessory phase during dehydration at temperatures and pressure above 700 °C and 2 GPa, respectively, as proposed by Hermann and Green (2001) and Hermann (2002a, 2002b), will lead to a release of MREE into a fluid phase. However, disappearance of allanite due to dissolution in a coexisting melt at temperatures and pressures above 1,050 °C and 4.5 GPa, respectively, (Hermann 2002b) results in a strongly LREE-enriched melt.

Acknowledgements D.F. acknowledges generous funding from the European Union as a Marie-Curie Individual Fellow (contract no. ERBFMBICT 983374 to DF) and Deutsche Forschungsgemeinschaft (DFG grant Fr 557/17-1). D.F. would especially like to thank Martina Frei for the donation of a generous MF special research grant. The high-pressure experimental work was supported by Deutsche Forschungsgemeinschaft (DFG grant Wi 1934/1-1 to AW). D.F. likes to thank Claude Dalpé for assistance during LA-ICP-MS analysis. Antje Gebel provided the trace element analysis of starting materials, for which the authors are particularly thankful. The final shape of this manuscript significantly benefited from comments by Gerhard Franz and Jon Blundy as well as the thorough and constructive reviews of Stephan Klemme, Stephen Foley and an anonymous reviewer, which the authors greatly appreciate.

References

Beattie P, Drake M, Jones J, Leeman W, Longhi J, McKay G, Nielsen R, Palme H, Shaw D, Takahashi E, Watson B (1993) Terminology for trace element partitioning. Geochim Cosmochim Acta 57:1605–1606

Blundy JD, Wood BJ (1994) Prediction of crystal-melt partition coefficients from elastic moduli. Nature 372:452–454

Bonazzi P, Menchetti S (1995) Monoclinic endmembers of the epidote-group: effects of the $Al \leftrightarrow Fe^{3+} \leftrightarrow Fe^{2+}$ substitution and of the entry of REE^{3+}. Mineral Petrol 53:133–153

Bonazzi P, Menchetti S, Reinecke T (1996) Solid solution between piemontite and androsite-(La), a new mineral of the epidote group from Andros Island, Greece. Am Mineral 81:735–742

Bottazzi P, Tiepolo M, Vannucci R, Zanetti A, Brumm R, Foley SF, Oberti R (1999) Distinct site preference for heavy and light REE in amphibole and the prediction of $^{Amph/L}D_{REE}$. Contrib Mineral Petrol 137:36–45

Brice JC (1975) Some thermodynamic aspects of the growth of strained crystals. J Crystal Growth 28:249–253

Brooks CK, Henderson P, Rønsbo JG (1981) Rare-earth partition between allanite and glass in the obsidian of Sandy Braes, northern Ireland. Mineral Mag 44:157–160

Brunsmann A, Franz G, Erzinger J, Landwehr D (2000) Zoisite- and clinozoisite- segregations in metabasites (Tauern Window, Austria) as evidence for high-pressure fluid-rock interaction. J Metamorph Geol 18:1–21

Brunsmann A, Franz G, Heinrich W (2002) Experimental determination of zoisite-clinozoisite phase equilibria in the system $CaO–Al_2O_3–Fe_2O_3–SiO_2–H_2O$. Contrib Mineral Petrol 143:115–130

Carcangiu G, Palomba M, Tamanini M (1997) REE-bearing minerals in the albitites of Central Sardinia, Italy. Mineral Mag 61:271–283

Cressey G, Steel AT (1988) An EXAFS study on Gd, Er and Lu site location in the epidote structure. Phys Chem Minerals 15:304–312

Dollase WA (1968) Refinement and comparison of the structure of zoisite and clinozoisite. Am Mineral 53:1882–1898

Dollase WA (1969) Crystal structure and cation ordering of piemontite. Am Mineral 54:710–717

Dollase WA (1971) Refinement of the crystal structures of epidote, allanite and hancockite. Am Mineral 56:447–464

Enami M, Banno S (1999) Major rock forming minerals in UHP metamorphic rocks. Int Geol Rev 41:1058–1066

Evans BW, Vance JA (1987) Epidote phenocrysts in dacitic dikes, Boulder County, Colorado. Contrib Mineral Petrol 96:178–185

Exley RA (1980) Microprobe studies of REE-rich accessory minerals: Implications for Skye granite petrogenesis and REE mobility in hydrothermal systems. Earth Planet Sci Lett 48:97–110

Fleet ME, Pan Y (1995) Crystal chemistry of rare earth elements in fluorapatite and some calc-silicates. Eur J Mineral 7:591–605

Franz G, Smelik EA (1995) Zoisite-clinozoisite bearing pegmatites and their importance for decompressional melting in eclogites. Eur J Mineral 7:1421–1436

Gabe EJ, Portheine JC, Withlow SH (1973) A reinvestigation of the epidote structure: confirmation of the iron location. Am Mineral 58:218–223

Grauch RI (1989) Rare earth elements in metamorphic rocks. In: Lipin BR, McKay GA (eds) Geochemistry and mineralogy of rare earth elements. Rev Mineral 21:147–167

Grevel KD, Nowlan EU, Fasshauer DW, Burchard M (2000) In situ X-ray diffraction investigation of lawsonite and zoisite at high pressures and temperatures. Am Mineral 85:206–216

Grew ES, Essene EJ, Peacor DR, Su SC, Asami M (1991) Dissakisite-(Ce), a new member of the epidote-group and the Mg-analogue of allanite-(Ce) from Antarctica. Am Mineral 76:1990–1997

Hazen RM, Finger LW (1979) Bulk-modulus volume relationship for cation-anion polyhedra. J Geophys Res 84:6723–6728

Henderson P (1982) Inorganic geochemistry. Pergamon Press, Oxford, 353 pp

Hermann J, Green DH (2001) Experimental constraints on high pressure melting in subducted crust. Earth Planet Sci Lett 188:149–168

Hermann J (2002a) Experimental constraints on phase relations in subducted oceanic crust. Contrib Mineral Petrol 143:219–235

Hermann J (2002b) Allanite: thorium and light rare earth element carrier in subducted crust. Chem Geol (in press)

Hickmott DD, Sorensen SS, Rogers PSZ (1992) Metasomatism in a subduction complex: constraints from microanalysis for trace elements in minerals from garnet amphibolite from the Catalina Schist. Geology 20:347–350

Keane SD, Morrison J (1997) Distinguishing magmatic from subsolidus epidote: laser probe oxygen isotope compositions. Contrib Mineral Petrol 126:265–274

Liebscher A, Gottschalk M, Franz G (2002) The substitution Fe^{3+}-Al and the isosymmetric displacive phase transition in synthetic zoisite: a powder X-ray and infrared spectroscopy study. Am Mineral 87:909–921

Mahood G, Hildreth W (1983) Large partition coefficients for trace elements in high silica ryholites. Geochim Cosmochim Acta 47:11–30

Moench RH (1986) Comments and reply on "Implications of magmatic epidote-bearing plutons on crustal evolution in the accreted terranes of northwestern North America" and "Magmatic epidote and its petrologic significance." Geology 14:188–189

Nagasaki A, Enami M (1998) Sr-bearing zoisite and epidote in ultra-high pressure (UHP) metamorphic rocks from the Su-Lu province, eastern China: an important Sr reservoir under UHP conditions. Am Mineral 83:240–247

Nagasawa H (1966) Trace element partition coefficient in ionic crystals. Science 152:767–769

Nystrom JO (1984) Rare earth element mobility in vesicular lava during low-grade metamorphism. Contrib Mineral Petrol 88:328–331

Onuma N, Higuchi H, Wakita H, Nagasawa H (1968) Trace element partition between two pyroxenes and the host lava. Earth Planet Sci Lett 5:47–51

Pan Y, Fleet ME (1996) Intrinsic and external controls on the incorporation of rare-earth elements in calc-silicate minerals. Can Mineral 34:147–159

Peacor DR, Dunn PJ (1988) Dollaseite-(Ce) (magnesium orthite refined): Structure refinement and implications for the $F^{+} + M^{2+}$ substitution in epidote-group minerals. Am Mineral 73:838–842

Poli S, Schmidt MW (1998) The high-pressure stability of zoisite and phase relations of zoisite bearing assemblages. Contrib Mineral Petrol 130:162–175

Press WH, Teukolsky SA, Vetterling WT, Flannery BP (1992) Numerical recipes in C. Cambridge University Press, London, 965 pp

Sakai C, Higashino T, Enami M (1984) REE-bearing epidote from Sanbagawa pelitic schists, central Shikoku, Japan. Geochem J 18:45–53

Sawka WN (1988) REE and trace element variations in accessory minerals and hornblende from the strongly zoned McMurray Meadows Pluton, California. Trans R Soc Edinb Earth Sci 79:157–168

Shannon RD (1976) Revised ionic radii and systematic studies of interatomic distances in halides and chalcogenides. Acta Crystall A32:751–767

Shaw CSJ (1999) Dissolution of orthopyroxene in basanitic magma between 0.4 and 2 GPa: further implications for the origin of Si-rich alkaline glass inclusions in mantle xenoliths. Contrib Mineral Petrol 135:114–132

Skjerlie KP, Patino Douce AE (2002) The fluid-absent partial melting of a zoisite-bearing quartz eclogite from 1.0 to 3.2 GPa; implications for melting in thickened continental crust and for subduction-zone processes. J Petrol 43:291–314

Smyth JR, Bish DL (1988) Crystal structures and cation sites of the rock-forming minerals. Allen and Unwin, Boston, 332 pp

Sorensen SS (1991) Petrogenetic significance of zoned allanite in garnet amphibolites from a paleo-subduction zone: Catalina Schist, southern California. Am Mineral 76:589–601

Sorensen SS, Grossman JN (1989) Enrichment of trace elements in garnet amphibolites from paleo-subduction zone: Catalina Schist, southern California. Geochim Cosmochim Acta 53:3155–3177

Sorensen SS, Grossman JN (1993) Accessory minerals and subduction zone metasomatism: a geochemical comparison of two melanges (Washington and California, U.S.A.). Chem Geol 110:269–297

Spear FS (1993) Metamorphic phase equilibria and pressure–temperature-time paths. Mineralogical Society of America Monographs, I, 799 pp

Tribuzio R, Messiga B, Vannucci R, Bottazzi P (1996) Rare earth element redistribution during high pressure low temperature metamorphism in ophiolitic Fe-gabbros (Liguria, northwestern Italy): Implications for light REE mobility in subduction zones. Geology 24:711–714

Tulloch AJ (1986) Comments and reply on ''Implications of magmatic epidote-bearing plutons on crustal evolution in the accreted terranes of northwestern North America'' and ''Magmatic epidote and its petrologic significance.'' Geology 14:188–189

Wood BJ, Blundy JD (1997) A predictive model for rare earth element partitioning and anhydrous silicate melts. Contrib Mineral Petrol 129:166–181

Zack T, Foley SF, Rivers T (2002) Equilibrium and disequilibrium trace element partitioning in hydrous eclogites (Trescolmen, Central Alps). J Petrol 43:1947–1974

Zen E-an (1985) Implications of magmatic epidote-bearing plutons on crustal evolution in the accreted terranes of northwestern North America. Geology 13:266–269

Zen E-an, Hammarstrom JM (1984) Magmatic epidote and its petrologic significance. Geology 12:515–518

Zen E-an, Hammarstrom JM (1986) Comments and reply on ''Implications of magmatic epidote-bearing plutons on crustal evolution in the accreted terranes of northwestern North America'' and ''Magmatic epidote and its petrologic significance.'' Geology 14:188–189